scientific reports

Check for updates

OPEN

Projecting groundwater flood risk in a lowland karst system under future climates

Ruhhee Tabbussum[1,4]✉, Bidroha Basu[2], Patrick Morrissey[1], Conor Murphy[3] & Laurence Gill[4]

Future flood dynamics in a lowland karst catchment draining into Galway Bay, Ireland, have been assessed under climate-change scenarios. Bayesian neural network model (BNN) was calibrated on 1980–2015 observations of rainfall, tides, and turlough flood volumes, yielding correlations of $R = 0.95$ (training) and $R = 0.78$ (overall). Projections driven by CORDEX under RCP 4.5 and 8.5 for 2016–2100 reveal ensemble-mean rainfall increases of 1.2 mm decade^{-1} and 2.5 mm decade^{-1}, respectively, corresponding to flood-volume growth rates of 5×10^6 m^3 decade^{-1} and 1.1×10^7 m^3 decade^{-1}. Wavelet coherence indicated high-frequency coupling (> 0.7) between rainfall and floods under RCP 8.5 versus < 0.5 under RCP 4.5. Extreme-event analysis showed a 40% rise in joint 95th -percentile rainfall and flood-volume events under RCP 8.5 ($p < 0.05$). Generalized extreme-value fits to annual maxima for 2018–2037 versus 2080–2099 project that a historical 100-year storm becomes 1-in-16-year event under RCP 8.5. 10-year rolling 90th -percentile analysis revealed rapid intensification of upper-tail floods under RCP 8.5 than RCP 4.5. These findings demonstrated that high-emission pathways substantially amplify flood magnitudes and frequencies and underscores the utility of integrated statistical and machine-learning frameworks for robust flood-risk assessment and climate-adaptation planning.

Keywords Bayesian neural network modelling, Climate projections, Extreme events, Karst flooding, Representative concentration pathways, Wavelet coherence

Flooding is a pressing global issue, exacerbated by the increasing intensity and variability of rainfall patterns due to climate change[1]. Coastal and low-lying regions face compounded risks from tidal influences and groundwater-surface water interactions (particularly in karst areas), with the resulting flood events leading to catastrophic social, economic, and ecological impacts[2]. Karst landscapes are particularly prone to groundwater flooding because these aquifers have limited storage capacity and rapidly transmit water through dissolutionally enlarged pathways (conduits)[3]. Groundwater flooding in karst systems is notably difficult to characterise due to its unpredictable spatial and temporal heterogeneity of flow through underground fractures and channels[4]. In karst groundwater systems, water levels can surge dramatically during heavy or extended rainfall. When underground storage and drainage capacities are exceeded, the water table may rise to the surface, causing flooding[5]. However, unlike the continuous flooding seen along rivers or coastlines, groundwater flooding in karst landscapes tends to be irregular and influenced by the varying hydrodynamic characteristics of the system. It typically appears only during extreme weather events and at infrequent intervals[6]. Climate projections suggest that changes in precipitation patterns and intensity will lead to more frequent and severe extreme events in Ireland leading to groundwater flooding[7]. Effective flood risk assessment and management require sophisticated modelling approaches to predict future flood dynamics under changing climatic conditions[8]. These efforts are especially crucial for long-term adaptation planning in regions experiencing amplified hydrological variability[9]. Traditional hydrological models, while valuable, often struggle to represent the nonlinear and dynamic relationships between rainfall, tidal level, and groundwater flooding, particularly under the influence of climate change[10].

The increasing availability of high-resolution climate datasets, such as those from the Coordinated Regional Climate Downscaling Experiment (CORDEX), provides more robust predictive modelling opportunities[11]. However, leveraging these datasets effectively requires methodologies capable of integrating complex

[1]Department of Civil, Structural and Environmental Engineering, Trinity College Dublin, The University of Dublin, Dublin, Ireland. [2]Department of Civil, Structural and Environmental Engineering, Munster Technological University, Cork, Ireland. [3]Irish Climate Analysis and Research Unit, Department of Geography, Maynooth University, Kildare, Ireland. [4]Department of Civil Engineering and Construction, Atlantic Technological University Sligo, Sligo, Ireland. ✉email: ruhhee.tabbussum@atu.ie

interactions across multiple variables and time scales[12]. This is particularly crucial in karst hydrology, where the high degree of subsurface heterogeneity, resulting from features such as dissolution-enlarged conduits, fractures, and sinkholes, leads to highly non-linear and variable flow dynamics[13]. Traditional hydrological models often struggle to accurately represent these systems due to their spatial discontinuity and duality of flow paths[14]. Consequently, various modelling strategies have emerged, ranging from conceptual lumped models to distributed and semi-distributed approaches that incorporate geological and geomorphological information[15]. Hybrid models combining elements of surface and subsurface flow are also increasingly used to address the complexity inherent to karst systems[16].

Predicting future flood scenarios is a complex task due to the multifaceted interactions among climatic, hydrological, and geographical variables[17]. Neural networks, particularly Bayesian Neural Networks (BNNs), have emerged as powerful tools for handling the nonlinearities and uncertainties inherent in such predictions[18]. These models offer several advantages, including their ability to learn complex relationships, integrate multiple inputs, and provide probabilistic predictions that quantify uncertainty, making them well-suited for climate and flood modelling applications[19]. Unlike deterministic models, BNNs provide probabilistic outputs, enabling a deeper understanding of prediction confidence - a critical factor in flood risk management[20]. Flood dynamics are not only influenced by immediate rainfall events but also by the temporal and frequency-domain interactions between climatic and hydrological variables[21]. Groundwater flooding in particular, exhibits a strong dependence on antecedent conditions, such as long-term rainfall accumulation, elevated groundwater tables, and soil saturation levels, which can persist for weeks or months prior to an event[22]. Unlike fluvial flooding, which typically responds rapidly to high-intensity rainfall and catchment runoff, groundwater flooding arises from prolonged recharge periods that gradually exceed the storage capacity of aquifers, especially in low-lying or karstic areas with limited drainage potential[6]. This distinction underscores the importance of long-memory processes and cumulative hydrological responses in forecasting groundwater-related flood hazards. Wavelet coherence analysis is a robust technique for identifying such relationships, as it decomposes time-series data into time-frequency space, enabling the exploration of correlations over varying scales[23]. This method is particularly suited for analysing the influence of tidal and rainfall variability on total flood volumes, capturing both short-term fluctuations and long-term trends[24]. The methodology employed in this study is particularly well-suited to evaluating the combined influence of tidal dynamics and rainfall variability on flood responses, specifically through the quantification of total flood volumes. While traditional flood risk assessments typically focus on peak water levels or inundation extents, the current analysis adopts a volume-based approach due to the nature of the available data, which are derived from a physically based hydraulic model developed for a lowland karst catchment with a tidally influenced outlet[25]. This hydrological setting is relatively uncommon and presents a high degree of complexity due to the interactions between surface and subsurface processes and the influence of both antecedent groundwater conditions and tidal backwater effects[5]. In such environments, groundwater flooding is often governed by prolonged recharge and elevated antecedent moisture, leading to delayed but substantial flood responses not well captured by metrics focused solely on flood peaks[26]. Karst systems are typified by dual-flow behaviour, comprising both diffuse and conduit pathways that respond nonlinearly to hydrometeorological inputs and this duality further complicates flood prediction[27]. As such, analysing flood volumes provides a more process-representative metric for understanding hydrological responses in karstic, tidally influenced systems. Furthermore, identifying long-term trends in these volumes is critical for evaluating how flood risks may evolve under projected climate variability and change, particularly in systems where the response is modulated by slow-changing groundwater storage and periodic tidal forcing.

Trend analysis, a widely used statistical tool, identifies persistent increases or decreases in hydrological variables over time[28]. Climate change is unequivocally intensifying the frequency and magnitude of extreme weather events, including heavy rainfall, heatwaves, and tropical cyclones, driven by rising global temperatures and shifts in atmospheric circulation patterns[29]. Extreme precipitation events are a key concern due to their direct linkage to flooding, especially in regions where hydrological and meteorological variables interact synergistically to amplify flood risks[30]. These changes in precipitation extremes are consistent with the Clausius-Clapeyron relationship, which suggests that atmospheric water-holding capacity increases by approximately 7% per degree Celsius of warming, leading to more intense and concentrated rainfall events[31]. In Europe, changes in atmospheric river patterns have led to unprecedented rainfall, as seen during the 2021 floods in Germany and Belgium, which were attributed to climate change with high confidence[32].

This research aims to predict total flood volumes in Galway Bay, Ireland, using a Bayesian neural network developed with rainfall and tidal level inputs. By integrating rainfall projections from CORDEX and tidal level data (provided by Marine Institute, Galway) this study employs BNNs to model total flood volumes, offering a novel approach to flood volume prediction up to 2100 under RCP 4.5 and RCP 8.5 scenarios. The inclusion of eleven ensemble rainfall projections allows for a comprehensive representation of uncertainty, addressing the stochastic nature of future climatic conditions. This research was conducted on a lowland karst area that drains into Galway Bay, Ireland because this region exemplifies a unique combination of climatic, hydrological, and geomorphological characteristics that make it particularly susceptible to climate-induced groundwater flooding. The area is characterised as a low-lying coastal zone that is highly prone to groundwater-surface water interaction (i.e. flooding) from the underlying allogenic karst aquifer due to a combination of rainfall, tidal surges, and rising sea levels. The interplay of these factors creates a complex flooding regime resulting in a network of intermittent lakes called *turloughs* that warrants detailed investigation to enhance understanding and prediction[21]. The karst conduit aquifer, fed by allogenic recharge from low permeability Old Red Sandstone hills, introduces additional hydro(geo)logical complexity. The interaction between surface water and groundwater in karst systems makes it challenging to predict flood responses accurately. A Bayesian Neural Network (BNN) model, as used in this study, is well-suited to capturing these nonlinear relationships.

Wavelet coherence analysis is employed to investigate the temporal and frequency-domain relationships between these variables and to investigate the interconnectedness of rainfall, tidal level, and total flood volume, providing insights into their co-variability across multiple ensembles. This study analyses trends for each ensemble under RCP 4.5 and RCP 8.5 and offers critical insights into the potential trajectory of flood risks. Such analyses are essential for informing regional flood management strategies and infrastructure planning. Extreme flood events are disproportionately impactful, making their prediction and characterization a cornerstone of climate impact studies[33]. The 95th percentile analysis of rainfall and flood volume focuses on the upper tail of their distributions, capturing the most severe and rare events[34]. This method provides valuable insights into how the frequency and intensity of these extremes may shift under future climate[35]. By evaluating extreme event trends across all ensemble risks under RCP 4.5 and RCP 8.5 scenarios, this study contributes to a better understanding of potential future flood hazards, offering critical information for disaster preparedness and mitigation planning. By applying Bayesian neural-network forecasts, wavelet coherence, trend and multivariate regression analyses, GEV-based return-period modelling, and empirical CDF and boxplot diagnostics, this study enriches flood-risk assessment and delivers actionable insights for climate-adaptation and resilience planning.

Results

Bayesian neural network (BNN) flood model

The Bayesian Neural Network (BNN) flood model was developed using daily observed rainfall and tidal-level data for the period 2007–2016. Both contemporaneous inputs and lagged values up to four preceding days were included to represent nonlinear and time-dependent interactions between rainfall, tidal dynamics, and total groundwater flood volume. An independent dataset from 2016 to 2018 was reserved for validation to assess model generalisation beyond the calibration period. Following training, the BNN was forced with rainfall projections from CORDEX climate simulations and corresponding tidal-level projections to generate daily flood-volume time series for 11 ensemble realisations under RCP4.5 and RCP8.5 for the period 2016–2100. These simulations form the basis for analysing projected changes in extreme groundwater flooding.

Annual maxima and the frequency of extreme-flood days were analysed to characterise changes in high-impact flooding under future climate scenarios (Fig. 1). Figure 1a shows the location of the study area, while Fig. 1b,c summarise changes in annual maximum flood volume and the annual count of extreme-flood days, respectively, for ensemble-mean projections under RCP4.5 and RCP8.5. Figure 1b presents annual maximum daily flood volumes from 2016 to 2100. The time series is characterised by substantial interannual variability under both scenarios, with overlapping values throughout much of the century. Formal non-parametric Mann–Kendall testing indicates that monotonic trends in annual maxima are not statistically significant for either RCP4.5 or RCP8.5, reflecting the dominance of year-to-year variability. Nevertheless, comparison of ensemble-mean behaviour indicates that higher-emission conditions are associated with a greater occurrence of high-magnitude annual maxima, consistent with subsequent distributional and extreme-value analyses.

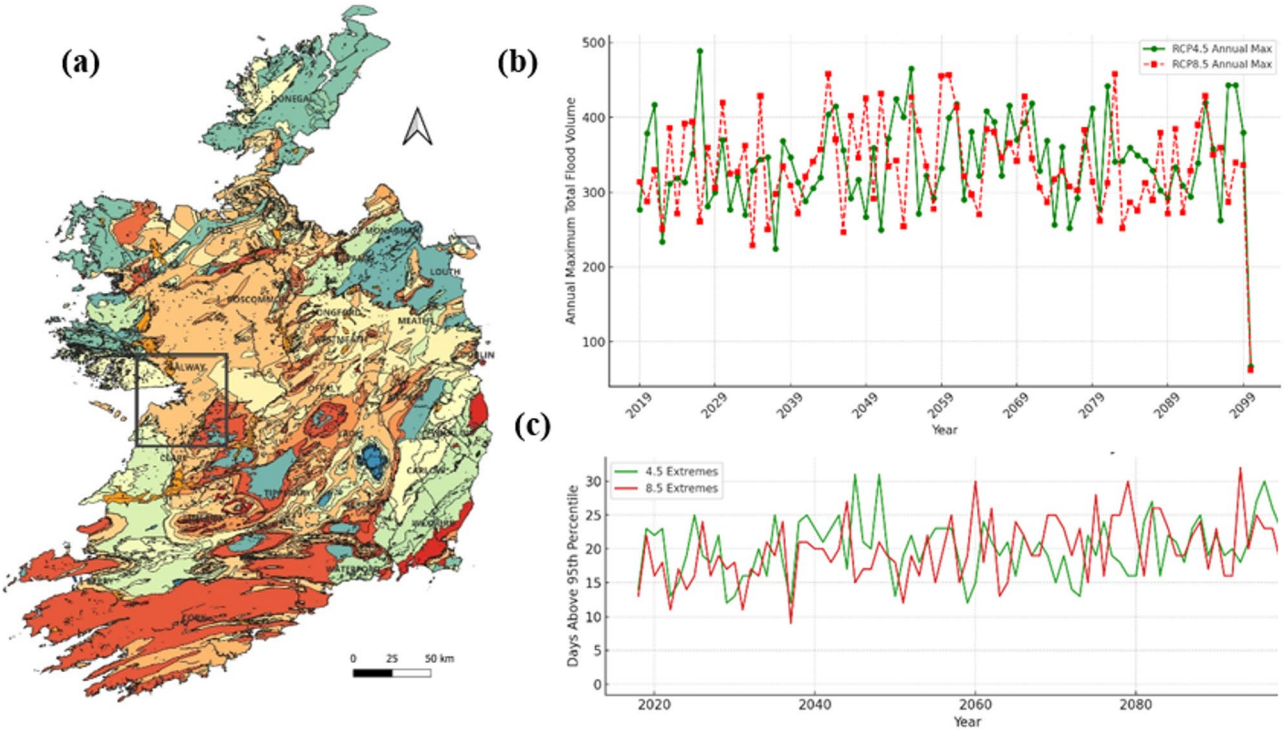

Fig. 1. (**a**) the location map of the study area, (**b**) the Annual Maxima (10^6 m^3) and (**c**) Annual Count of Extreme-Flood Days.

Figure 1c shows the annual number of days exceeding a fixed early-century (2016–2034) 95th-percentile flood-volume threshold. As with annual maxima, interannual variability is pronounced, and Mann–Kendall tests do not identify statistically significant monotonic trends in extreme-day counts under either scenario. However, relative differences between emission pathways are evident in the frequency distribution, with RCP8.5 exhibiting a greater tendency toward higher counts of extreme-flood days, particularly in later decades. This behaviour motivates further analysis using rolling percentiles, seasonal diagnostics, and extreme-value methods rather than reliance on linear trend detection alone.

Model performance is evaluated using independent validation, cross-validation, and regression diagnostics. During the independent validation period (2016–2018), the BNN reproduces interannual variability in annual flood volumes with an R^2 of 0.82 (Figure S21). Although the validation window is relatively short, this result indicates that the model generalises beyond the training data at annual time scales. When evaluated against the full observed dataset for 2007–2016 (Figure S22), strong agreement is observed between simulated and observed flood volumes (R^2 = 0.93; NSE = 0.93). The robustness of the calibration is further supported by the 5-fold cross-validation analysis of the 2007–2015 training dataset (Figure S23), for which performance metrics remain consistently high across folds ($R^2 \approx 0.996 \pm 0.0005$; NSE $\approx 0.996 \pm 0.0005$) with stable RMSE values. For the independent validation period (2016–2018), the model reproduces interannual variability at the annual scale (Figure S21; R^2 = 0.82). This short validation window is used solely to assess generalisation beyond the training period and is not intended to represent long-term predictive skill, which is instead evaluated through cross-validation and ensemble consistency.

Regression diagnostics illustrating model behaviour across the range of flood volumes are shown in Fig. 2. Figure 2a presents the regression plot for the training phase, where predicted and observed flood volumes exhibit a very strong linear relationship (correlation coefficient $R = 0.94791$) and closely follow the 1:1 reference line. The fitted regression for the training data is:

$$Output = 0.91 \times Target + 8 \times 10^6 \tag{1}$$

Post hoc ordinary least-squares analysis yields a slope of 0.910 (95% CI: 0.903–0.917; $p < 10^{-50}$) and an intercept of 8.0×10^6 m^3 (95% CI: 7.4–8.6 × 10^6; $p < 10^{-20}$), indicating minimal bias during calibration. Figure 2b presents the regression plot for the combined dataset (training, validation, and testing). While the relationship remains moderate to strong ($R = 0.77589$), increased scatter is evident, particularly at higher flood volumes. The fitted regression for the full dataset is:

$$Output = 0.8 \times Target + 3.6 \times 10^7 \tag{2}$$

Here, the slope decreases to 0.800 (95% CI: 0.776–0.824; $p < 10^{-30}$) and the intercept increases to 3.6×10^7 m^3 (95% CI: 3.2–4.0 × 10^7; $p < 10^{-15}$). The non-overlapping confidence intervals between Eqs. (1) and (2) confirm that this change is statistically robust and reflects a systematic underprediction of high-end flood volumes on unseen data. This behaviour, most evident at the upper tail in Fig. 2b, indicates that projected future extremes derived from the BNN should be interpreted as conservative estimates. Following evaluation, the trained model

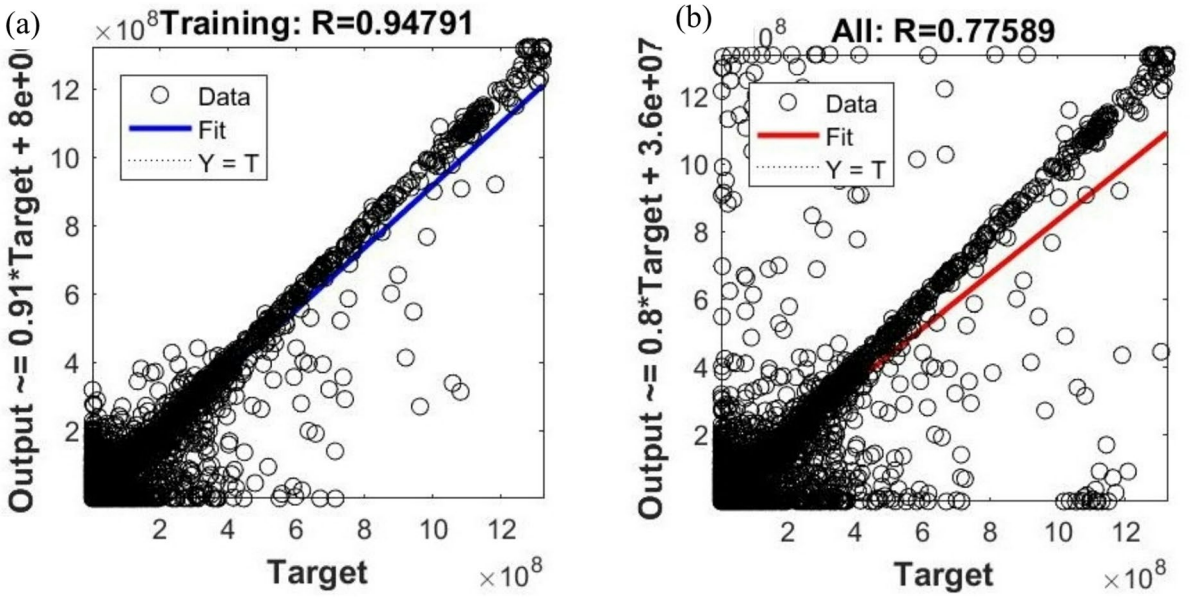

Fig. 2. Regression plots of the Bayesian Neural Network Model for the prediction of the total flood volume (**a**) Observed vs. predicted total flood volume on training data (**b**) Observed vs. predicted total flood volume–full dataset performance.

was driven with CORDEX rainfall projections and tidal projections to simulate future daily flood volumes for 11 ensembles under RCP 4.5 and RCP 8.5, generating projections to 2100. These simulations form the basis of the analyses below.

Evolution of the upper tail and seasonal structure of flood volumes

To assess changes in high-end flood behaviour beyond single annual extremes, Fig. 3a presents the 10-year rolling 90th percentile of daily flood volume under RCP4.5 and RCP8.5. This metric characterises frequent high-volume flooding within each moving decadal window while reducing sensitivity to isolated extreme years. Both emission scenarios exhibit increasing upper-tail flood volumes through the century; however, the increase is consistently larger and more rapid under RCP8.5, indicating a stronger upward shift in high-end flood behaviour under higher greenhouse-gas forcing.

Seasonal variations in flood behaviour are shown in Fig. 3b, which compares mean monthly flood volumes for early-century and late-century periods under both scenarios. Late-century flood volumes exceed early-century levels in most months, with the largest increases occurring during the established flood season. Under RCP8.5, increases are evident not only during peak flood months but also extend into shoulder seasons, indicating both intensification of seasonal maxima and a potential broadening of the flood-prone period.

Changes in the magnitude and variability of the most extreme events are further illustrated in Fig. 3c, which shows decadal distributions of annual maximum flood volumes. From the 2010 s to the 2090 s, the distributions shift progressively toward higher values under both scenarios, with a more pronounced upward shift under RCP8.5. In addition to increases in median annual maxima, the interquartile range and upper tails also expand under RCP8.5, indicating greater variability in extreme flood magnitudes in later decades.

Taken together, the rolling upper-percentile analysis (Fig. 3a), seasonal climatology (Fig. 3b), and decadal extreme distributions (Fig. 3c) consistently indicate a scenario-dependent intensification of upper-tail groundwater flooding. While increases are evident under both emission pathways, changes are systematically larger under RCP8.5, affecting the frequency, magnitude, and seasonal expression of high-volume flood events.

It is important to note that the 10-year rolling 90th percentile shown in Fig. 3a represents a windowed upper-tail statistic rather than an instantaneous annual trend. Consequently, values in the early part of the record already reflect aggregated variability from the late-2010s and early-2020s and may exhibit separation before long-term forcing differences fully emerge. In groundwater-dominated karst systems, small differences in rainfall intensity, sequencing, and antecedent wetness can be amplified through nonlinear storage–discharge responses, leading to visible divergence in upper-tail flood metrics even when mean conditions remain similar. This early separation is consistent with ensemble-mean rainfall trend differences of 40–60% steeper slopes under RCP8.5 and with decadal increases of 20–40 mm in antecedent 30-day rainfall totals, which precondition the system toward higher flood response.

Seasonal–interannual evolution of monthly peak flood volumes

To examine how extreme flood magnitudes evolve jointly across seasons and through time, monthly peak flood volumes were summarised using heat maps. Figure 4 presents heat maps of monthly peak flood volumes from 2016 to 2100 under RCP4.5 and RCP8.5, where years are arranged vertically and months horizontally, allowing simultaneous assessment of temporal trends and seasonal structure.

Under RCP4.5, the heat map shows relatively moderate monthly peak flood volumes during the early decades (approximately 2016–2030), with cooler colour tones across most months (Fig. 4a). Over subsequent decades, warmer colours gradually emerge in the core flood-season months (approximately November–February), indicating increasing monthly peak flood volumes. However, this intensification is progressive rather than abrupt, and dry-season months (e.g. May–August) exhibit comparatively little change over the century.

In contrast, the RCP8.5 heat map (Fig. 4b) displays a stronger and earlier intensification of monthly peak flood volumes. By mid-century, peak-season months show distinctly warmer colours than under RCP4.5, reflecting substantially larger monthly flood peaks. In addition, the intensification extends into shoulder months such as October and March, indicating an expansion of the period during which high flood volumes occur. By the late century (approximately 2080–2100), most winter-season months under RCP8.5 reach the highest colour bands, highlighting a pronounced amplification of extreme monthly flood volumes under high greenhouse-gas forcing.

Taken together, the heat maps indicate a clear scenario-dependent evolution in both the magnitude and seasonal extent of extreme flooding. While RCP4.5 is characterised by gradual increases largely confined to the core flood season, RCP8.5 exhibits stronger intensification, earlier emergence of high monthly peaks, and a broader seasonal window of elevated flood risk.

Time–frequency attribution using wavelet coherence

To examine how the coupling between hydro-climatic drivers and flood response evolves across time scales, we applied wavelet coherence analysis between (i) rainfall and flood volume, and (ii) tidal level and flood volume, using BNN-simulated flood volumes for each scenario. Wavelet coherence quantifies the strength of association in the time–frequency domain; it supports inference about scale-dependent coupling but does not establish causality. Wavelet coherence analysis was performed in this study to explore the dynamic, time-varying relationships between key variables—rainfall, tidal volume, and total flood volume—over a range of temporal scales[36]. The use of this technique is particularly suited for analysing the complex interplay between these variables under future climate scenarios[37]. Flooding in the lowland karst area of south Galway arises from the interplay between rainfall, tidal dynamics, and other climatic factors[38]. These relationships are often nonlinear and occur at multiple temporal scales, from daily patterns to seasonal and multi-decadal variations[39]. Wavelet coherence allows for the identification of such multi-scale relationships, providing insights into how these factors interact over time[40]. By applying wavelet coherence analysis to the outputs generated by the Bayesian

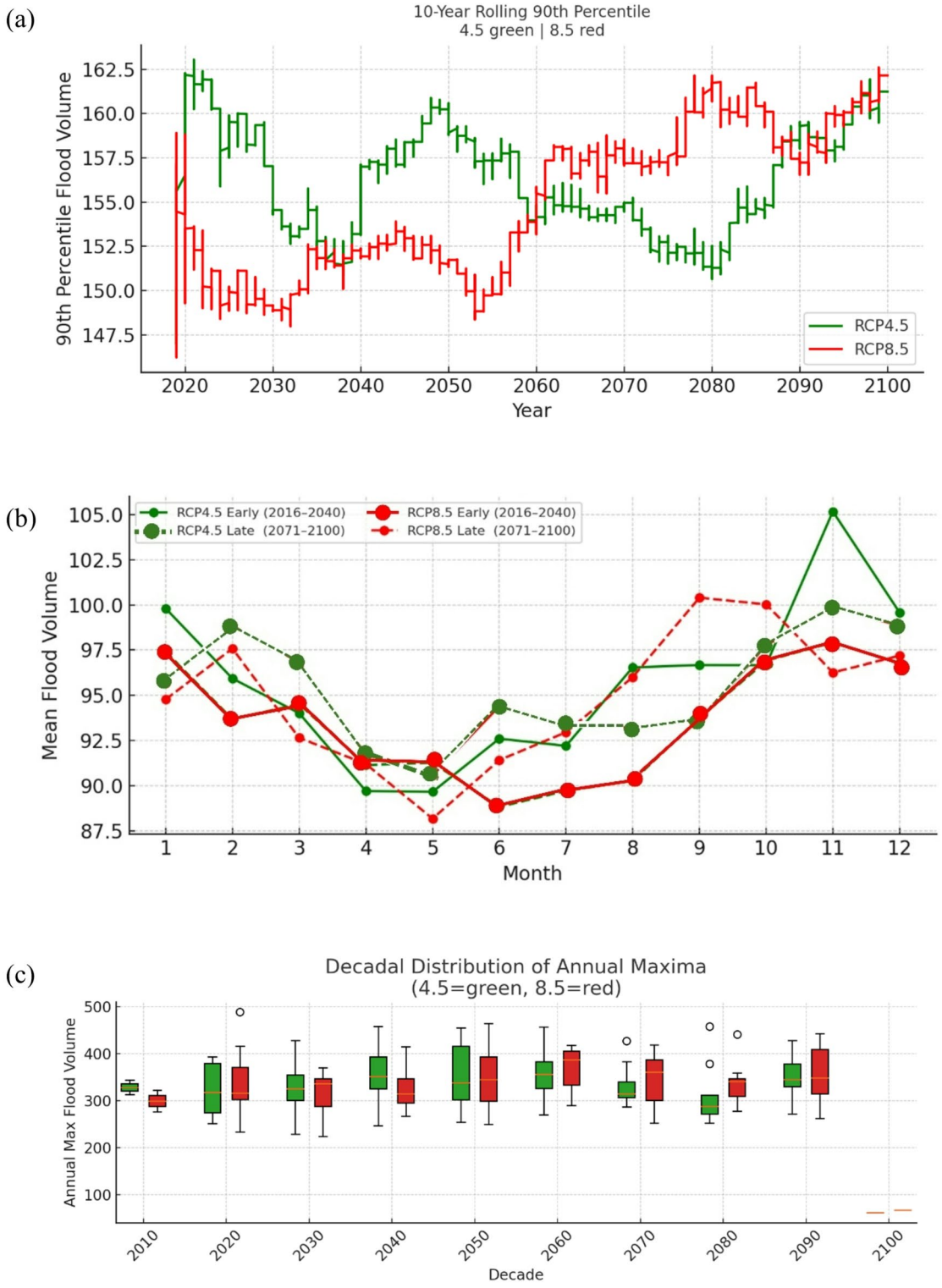

Fig. 3. (**a**) 10-Year Rolling 90th Percentile (RCP4.5 green, RCP8.5 red) illustrating upper-tail behaviour within moving decadal windows rather than year-by-year trends; (**b**) Seasonal Climatology-10^6 m^3 (RCP4.5 green, RCP8.5 red; solid=early, dashed=late) (**c**) Decadal Distribution of Annual Maxima-10^6 m^3 (4.5 green, 8.5 red) showing shifts in median, spread, and upper extremes across emission pathways.

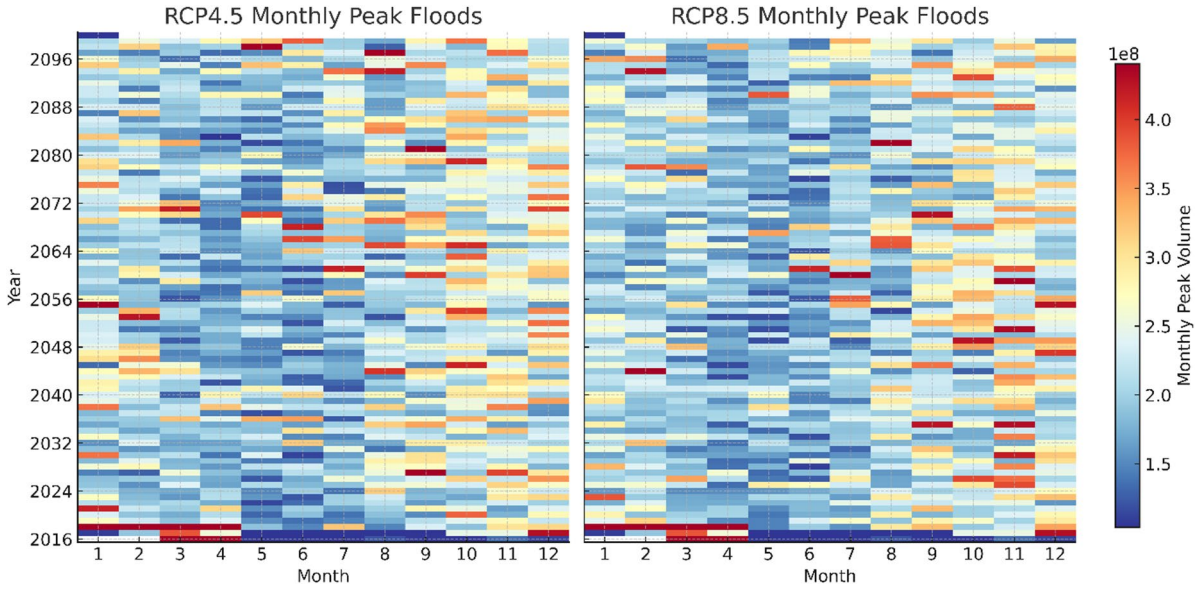

Fig. 4. Heat Maps of Monthly Peak Flood Volumes (2016–2100) under RCP4.5 and RCP8.5 Scenarios.

Neural Network (BNN) model for RCP 4.5 and RCP 8.5 scenarios, the study investigates how the coherence between rainfall/tidal level and total flood volume evolves under future climate conditions. This is crucial for understanding potential shifts in flood risk drivers due to climate change.

Figure 5 (Ensemble 1) indicates that rainfall–flood coherence under RCP4.5 is moderate at interannual to decadal periods (~1–10 years) and strengthens later in the century at longer periods. Under RCP8.5, rainfall–flood coherence is stronger and more persistent across multiple scales, including prominent coherence at 1–5-year periods across much of the century and strengthening after ~2060. These results are consistent with a larger role for rainfall variability and extremes under higher forcing.

From Fig. 5a, rainfall–flood coherence under RCP 4.5 is moderate at interannual to decadal periods (roughly 1–10 years) across much of the century, with clearer strengthening after 2060 at longer periods approaching multi-decadal scales. This suggests that under stabilised emissions, rainfall becomes a more consistent driver of long-term flood dynamics in the latter half of the century. Figure 5b highlights that under RCP 8.5 the rainfall–flood coherence is both stronger and more persistent across multiple timescales. Elevated coherence is observed at 1–5 years throughout the century, and a pronounced intensification emerges beyond 2060. This indicates that in a high-emissions scenario, flood volumes are more directly and consistently coupled with rainfall variability, reflecting the amplified role of precipitation extremes in a warmer climate.

Figure 5c shows that the tide–flood relationship under RCP 4.5 is weak at shorter scales but becomes more evident after 2060 at decadal periods. This points to tides as a secondary influence that only becomes noticeable once emissions stabilise and longer-term variability is expressed. By contrast, Fig. 5d demonstrates that under RCP 8.5 the tidal influence strengthens more substantially, particularly at 5–20 year scales after mid-century. This pattern is consistent with the projected rise in mean sea level and greater tidal forcing under high-emission conditions. Tide–flood coherence is generally weaker than rainfall–flood coherence, but under RCP8.5 it becomes more evident at multi-year to decadal scales (e.g., ~5–20 years after mid-century), consistent with an increasing influence of tidal dynamics and sea-level-related boundary conditions on flood response.

The ensemble spread (Figures S1–S10) reinforces these patterns. Rainfall–flood coherence is consistently higher under RCP 8.5 across most ensembles, with Ensembles 1, 5, and 10 showing particularly strong and persistent coherence across all timescales. In contrast, Ensembles 2 and 7 display weaker rainfall–flood coherence at shorter periodicities, highlighting regional or model-specific variability in rainfall-driven flooding. Tide–flood coherence exhibits greater variability across ensembles: in Ensembles 3, 6, and 9, tidal contributions are markedly amplified under RCP 8.5 compared to RCP 4.5, suggesting that particular configurations may accentuate tidal effects. Other ensembles, however, show only modest tidal influence, confirming that while tides can enhance flood risk, rainfall remains the dominant control.

Together, these results underscore three consistent messages. First, rainfall is the primary driver of groundwater flood dynamics in the south Galway karst system, and its influence strengthens under climate change. Second, tidal effects, though secondary, can become amplified under RCP 8.5, particularly in some ensemble realisations, implying that sea-level rise and tidal variability cannot be ignored in risk assessments. Third, the coherence patterns across Ensembles 1–10 provide a robust indication that emission pathways strongly shape the degree of coupling between hydro-climatic drivers and flood responses. Overall, the amplified coherence under RCP 8.5 highlights the compounded risk of rainfall and tidal influences acting together in a warmer climate. This underscores the urgency of both climate mitigation and adaptation, as stabilising emissions (RCP 4.5) clearly reduces the strength and persistence of these relationships.

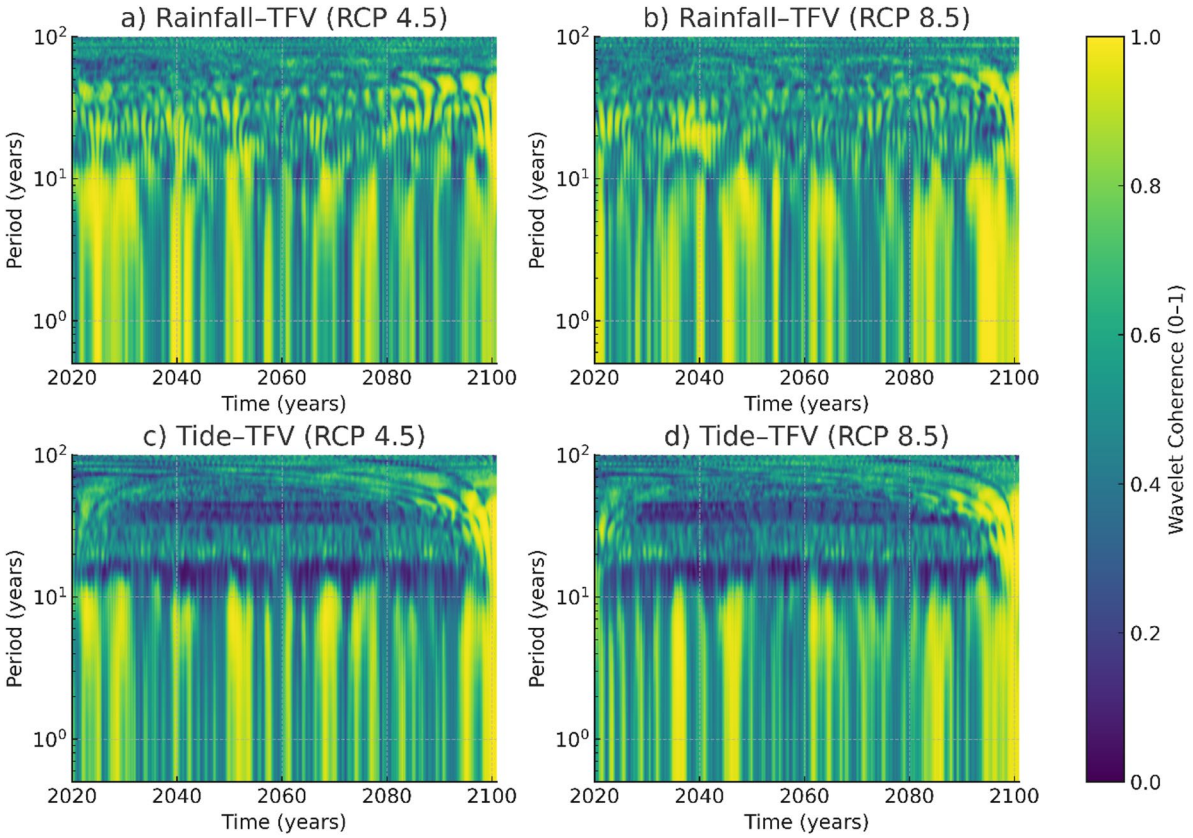

Fig. 5. Wavelet Coherence plots from 2020 to 2100 between: (**a**) Rainfall and Total Flood Volume for RCP 4.5 Ensemble 1 (**b**) Rainfall and Total Flood Volume for RCP 8.5 Ensemble 1 (**c**) Tidal Level and Total Flood Volume for RCP 4.5 Ensemble 1 (**d**) Tidal Level and Total Flood Volume for RCP 8.5 Ensemble 1.

Statistical relationships between rainfall, antecedent conditions, and flood response under future climates: trends in rainfall and total flood volume

Long-term trends in rainfall and corresponding total flood volumes were analysed for the period 2020–2100 using CORDEX rainfall projections and BNN-simulated flood volumes. Figure S18 illustrates representative trend relationships for Ensembles 1, 3, and 11, while results for the remaining ensembles are provided in Figure S11. Under RCP4.5, rainfall exhibits consistent seasonal variability through the century with only modest increases in peak-season intensity. Corresponding flood volumes display variability that broadly tracks rainfall peaks but show relatively stable long-term behaviour. In contrast, under RCP8.5, rainfall trends exhibit stronger variability and higher peak intensities, particularly in the latter half of the century. Flood volumes under RCP8.5 show larger variability and higher peaks that coincide with periods of enhanced rainfall intensity, indicating stronger amplification of flood response under high-emissions forcing.

Ordinary least-squares regressions were fitted to smoothed flood-volume time series for each ensemble. For Ensemble 6, the RCP4.5 trend has a slope of 0.008×10^8 m^3 per decade ($R^2 = 0.31$, $p < 0.001$), whereas under RCP8.5 the slope increases to 0.012×10^8 m^3 per decade ($R^2 = 0.44$, $p < 0.001$), representing an approximately 50% increase in trend magnitude. Ensembles 1 and 11 show similar behaviour, with 40–60% increases in slope under RCP8.5 relative to RCP4.5 and corresponding increases in explained variance ($\Delta R^2 \approx 0.10$–0.15). Averaged across all ensembles, the RCP8.5 flood-volume trend is 0.011×10^8 m^3 per decade, compared with 0.007×10^8 m^3 per decade under RCP4.5.

Decadal evolution of antecedent wetness conditions

To assess changes in baseline hydrological conditions preceding flood events, rolling 30-day antecedent rainfall totals were computed and summarised by decade under both emission scenarios. Results for Ensembles 6 and 8 are shown in Fig. 6, with additional ensembles provided in Figure S13. During the early decades (2010–2030 s), median antecedent rainfall distributions under RCP4.5 and RCP8.5 are similar. From the mid-century onward (2040–2060 s), distributions under RCP8.5 shift upward more strongly than those under RCP4.5. By the late century, median 30-day antecedent rainfall under RCP8.5 exceeds early-century levels by approximately 20–40 mm, indicating more persistently wet pre-conditioning states. Across most ensembles, RCP8.5 distributions consistently lie above RCP4.5 distributions from mid-century onward, reflecting wetter baseline conditions prior to flood events.

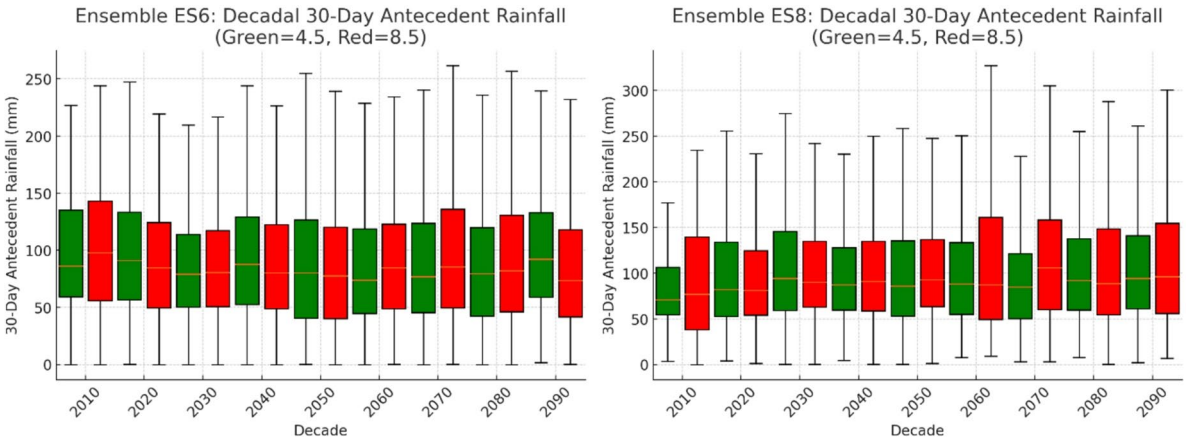

Fig. 6. Decadal 30-day antecedent rainfall distributions under RCP4.5 (green) and RCP8.5 (red).

Dependence of extreme floods on antecedent rainfall windows

The influence of antecedent wetting duration on extreme flood generation was examined by relating high-volume flood days to cumulative rainfall windows of 7, 14, and 30 days. Results for Ensemble ES6 are shown in Fig. 7. Scatter plots of flood volume versus antecedent rainfall indicate that shorter accumulation windows exert stronger control on extreme flood magnitudes. For ES6, the fitted slope between flood volume and rainfall decreases systematically with window length: 6.6×10^{6} m^3 mm^{-1} for 7 days, 2.1×10^{6} m^3 mm^{-1} for 14 days, and 0.56×10^{6} m^3 mm^{-1} for 30 days. Correlation analysis across rainfall windows (Fig. 7d) shows a maximum association at approximately 3–4 days ($r\approx0.21$), with correlations decreasing gradually for longer windows. This indicates that rainfall accumulated over several days immediately preceding an event exerts the strongest influence on peak groundwater flood volumes in this ensemble.

Extreme rainfall and flood event characteristics

Extreme rainfall and flood events were analysed using a 95th-percentile threshold applied to projections from 2020 to 2100 under both emission scenarios. Results for Ensembles 1 and 11 are shown in Fig. 8, with additional ensembles provided in Figure S12. Under RCP4.5, extreme rainfall events remain relatively stable in frequency and magnitude, with modest interannual variability. Extreme flood events closely track rainfall extremes but exhibit slightly higher variability due to additional hydrological controls. Under RCP8.5, extreme rainfall events become more frequent and intense, particularly in the latter half of the century. Corresponding flood volumes show higher peaks and increased event frequency, with strong correspondence between extreme rainfall and flood response. For Ensemble 1, maximum rainfall during extreme events under RCP8.5 exceeds RCP4.5 values by approximately 20–25%, while mean extreme flood volumes are approximately 30% higher under RCP8.5. Across ensembles, the frequency of extreme events increases by approximately 15–20% under RCP8.5 relative to RCP4.5. Trends in 95th-percentile rainfall and flood volumes are statistically significant ($p<0.05$) in the latter half of the century for most ensembles.

Decadal changes in extreme tidal conditions

Decadal changes in extreme tidal levels were examined using annual maximum daily peak tides, with results shown in Figure S14. In the 2020 s, median peak tides under RCP4.5 and RCP8.5 are nearly identical (≈0.183 m). From the 2030 s onward, median values under RCP8.5 increase relative to RCP4.5, with differences widening to approximately 0.005–0.01 m by the 2050–2060 s. Upper quartiles and whisker ranges under RCP8.5 also increase relative to RCP4.5, indicating more frequent extreme tidal peaks. By the 2080–2090 s, median annual peak tides under RCP8.5 are approximately 2–5% higher than under RCP4.5, with consistently higher upper extremes. Across full-decade comparisons, RCP8.5 produces larger extreme annual peak tides by approximately 0.001–0.003 m, indicating a progressive intensification of tidal extremes under higher emissions.

Discussion

This study integrates probabilistic flood modelling, ensemble climate projections, and multi-scale statistical analyses to examine how groundwater flood behaviour in a lowland karst system may evolve under contrasting emission pathways. By combining Bayesian Neural Network (BNN) simulations with trend analysis, wavelet coherence, antecedent rainfall diagnostics, and extreme-value modelling, the results provide a coherent picture of how both the magnitude and drivers of flooding respond to climate forcing.

Model performance and implications for future projections

The BNN framework enabled explicit representation of uncertainty arising from nonlinear hydrological responses and ensemble climate variability. Validation and cross-validation results demonstrate strong skill in reproducing observed flood volumes, while regression diagnostics highlight a systematic underprediction at the upper end of the flood-volume distribution on unseen data. This behaviour is consistent with known challenges

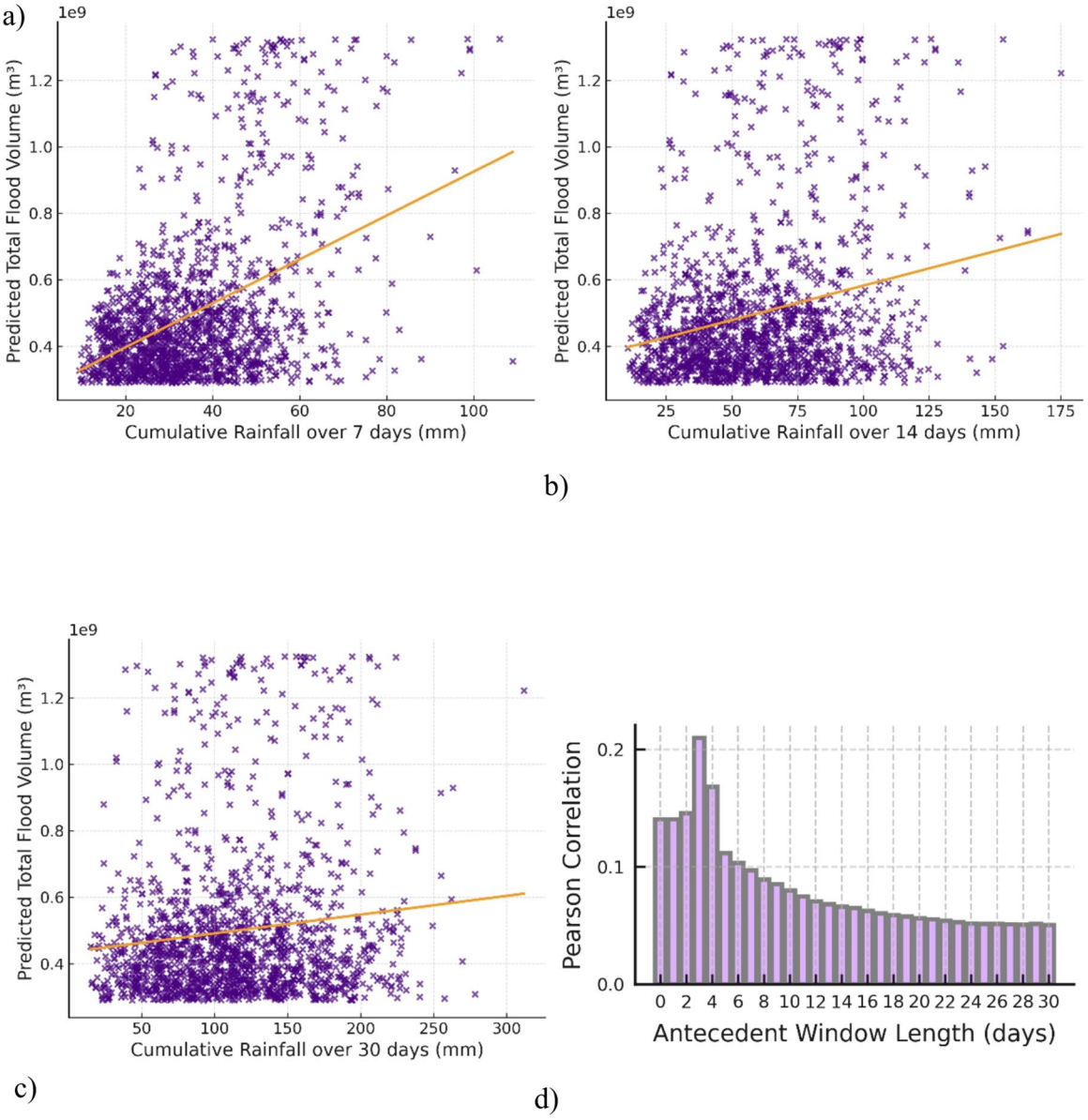

Fig. 7. Dependence of High-Volume Flood Peaks on Antecedent Rainfall Windows: (**a**) 7 days, (**b**) 14 days, and (**c**) 30 days for Ensemble ES6 (**d**) Ensemble ES6: Pearson Correlation between Flood Volume and Cumulative Antecedent Rainfall Windows (0–30 days).

in data-driven models when extrapolating rare extremes and implies that projected future flood volumes—particularly the largest events—should be interpreted as conservative estimates. The ensemble-based approach mitigates reliance on any single climate realisation and provides a more defensible basis for long-term flood-risk assessment than deterministic projections.

Emission pathway dependence of flood magnitude and frequency

Across all analyses, a consistent separation emerges between RCP4.5 and RCP8.5 futures. Upper-tail diagnostics—including annual maxima, rolling percentiles, and decadal distributions—indicate that both the frequency and magnitude of high-volume floods increase under warming, with systematically larger changes under RCP8.5. While RCP4.5 exhibits gradual increases largely confined to the core flood season, RCP8.5 is characterised by stronger amplification, earlier emergence of extremes, and an expansion of the flood-prone period into shoulder seasons. These patterns indicate that emission pathways influence not only how large floods become, but also how often high-impact conditions occur.

Time–frequency controls on groundwater flooding

Wavelet coherence analysis provides insight into how the coupling between hydro-climatic drivers and flood response evolves across temporal scales. Rainfall consistently emerges as the dominant control on groundwater

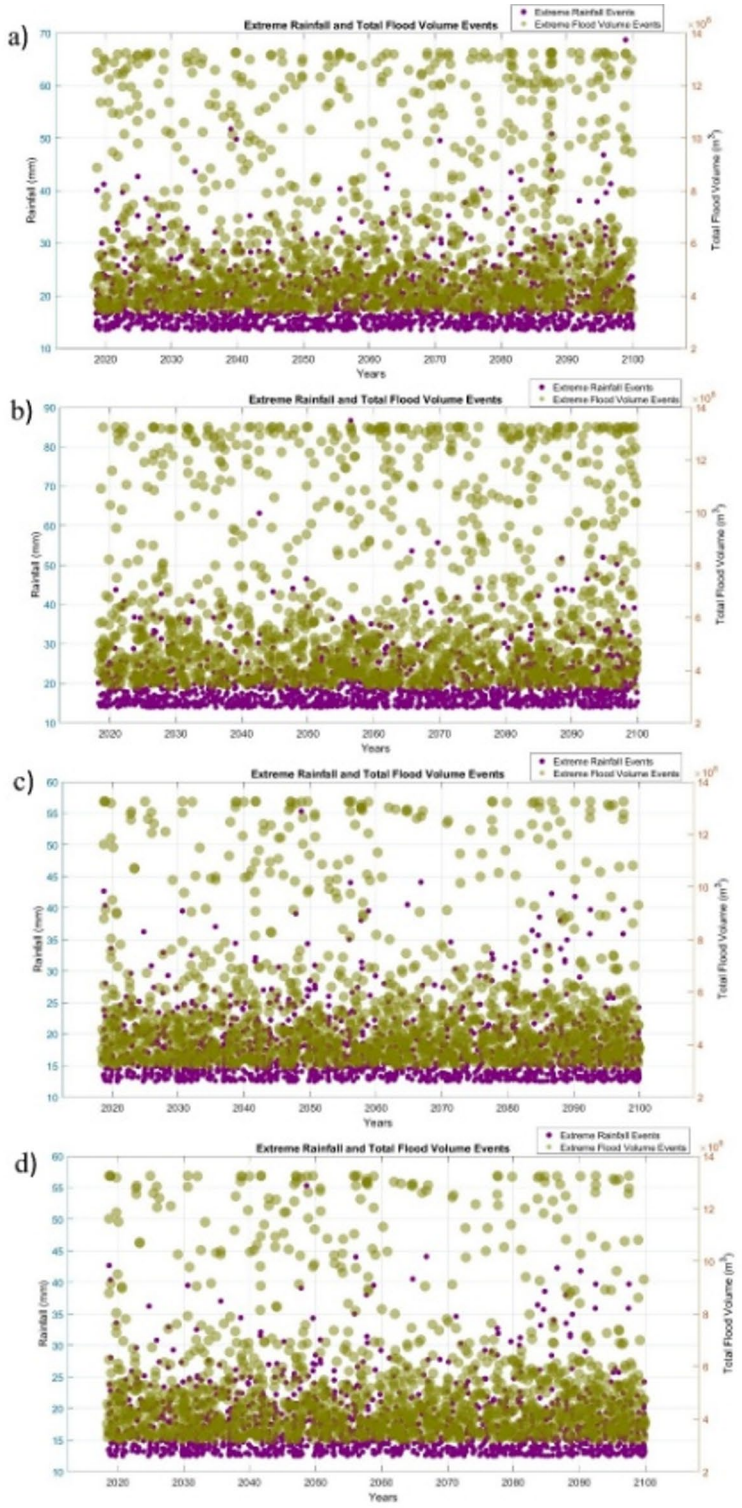

Fig. 8. Extreme Events (95th Percentile) of Rainfall and Total Flood Volume Climate Projections from 2020 AD up to 2100 AD (**a**) RCP 4.5 Ensemble 1 (**b**) RCP 8.5 Ensemble 1 (**c**) RCP 4.5 Ensemble 11 (**d**) RCP 8.5 Ensemble 11.

flooding, with stronger and more persistent coherence under RCP8.5 than under RCP4.5, particularly at interannual to decadal scales. This indicates that intensified rainfall variability under higher emissions increasingly governs flood behaviour across a range of time horizons.

Tidal influences are more variable and generally secondary but become more evident under RCP8.5 at longer time scales and in specific ensemble realisations. This suggests that while tides do not dominate flood generation,

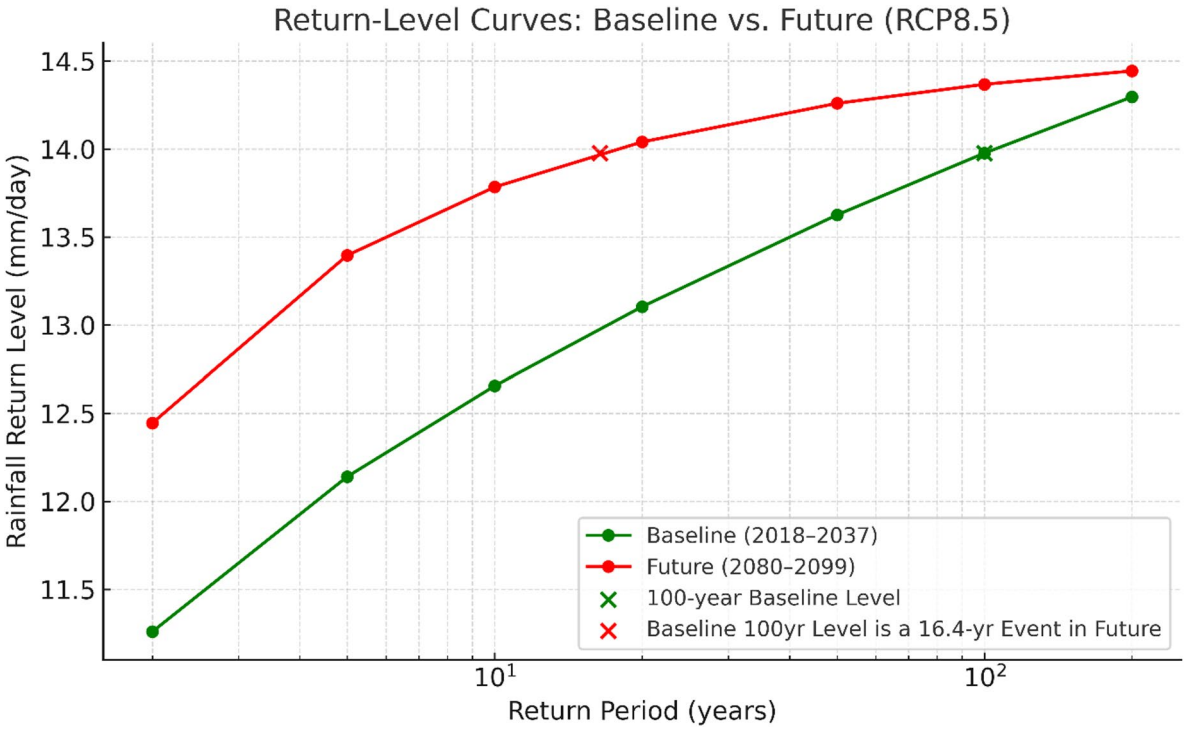

Fig. 9. Return-level curves: baseline vs. future (RCP8.5).

their contribution to flood variability may become more relevant under higher sea levels and enhanced coastal forcing, particularly when acting in combination with extreme rainfall.

Antecedent wetness and flood generation mechanisms

Analyses of antecedent rainfall reveal that groundwater flooding in this system is strongly conditioned by short-term pre-event wetting rather than long-duration accumulation alone. Correlation and slope analyses show that rainfall accumulated over several days immediately preceding an event exerts the strongest influence on extreme flood volumes, while longer accumulation windows dilute this signal. This behaviour is consistent with rapid saturation of shallow soils and karst conduits, where pre-conditioning over a few days governs the magnitude of flood response. Importantly, decadal shifts toward wetter baseline conditions under RCP8.5 indicate that such flood-prone states occur more frequently later in the century, increasing the likelihood that intense rainfall translates into large groundwater floods.

Extreme events, compounding drivers, and ensemble uncertainty

Extreme-event analysis further demonstrates a clear dependence on emission pathway. Under RCP8.5, extreme rainfall and flood events become both more frequent and more intense, with ensemble-mean increases of approximately 15–20% in event frequency and around 30% in mean extreme flood volume for representative ensembles. While ensemble-to-ensemble variability remains substantial—reflecting uncertainty in climate projections and hydrological sensitivity—the consistency of trends across ensembles lends confidence to the direction of change. The joint occurrence of extreme rainfall and elevated tidal conditions becomes more common under RCP8.5, increasing the potential for compound flooding, even though tidal amplitude itself remains largely stationary.

Tidal amplitude versus mean sea-level effects

The analysis of daily tidal amplitude indicates that the difference between high and low tide remains effectively constant through the century under both emission pathways. This finding implies that future increases in tidal flood risk are driven primarily by upward shifts in mean sea level and changes in storm conditions rather than by any systematic amplification of the tidal range itself. Consequently, compound flood risk arises from the coincidence of higher baseline sea levels with rainfall-driven groundwater flooding, rather than from expanding tidal swings.

Compression of extreme-event return periods

Extreme-value analysis based on the Generalized Extreme Value (GEV) distribution indicates a pronounced compression of return periods under RCP8.5 (Fig. 9). By the late century, a daily rainfall event historically associated with a 100-year return period is projected to occur on the order of once every 16 years under high-emission conditions. This change arises primarily from an increase in exceedance probability rather than from large increases in event magnitude, as reflected by the horizontal shift of the return-level curve. Consequently,

return periods derived from historical climate conditions are likely to underestimate the frequency of extreme rainfall events in a warmer climate.

Implications for flood-risk assessment

Taken together, the results indicate that future groundwater flood risk in lowland karst systems is shaped by a combination of intensified rainfall, more frequent wet antecedent conditions, and elevated baseline sea levels, with the strongest changes occurring under high-emission scenarios. While uncertainties across climate ensembles remain, the convergence of evidence across independent analyses—trend statistics, coherence patterns, antecedent diagnostics, and extreme-value modelling—supports the conclusion that both the likelihood and severity of flooding increase substantially under continued warming. These findings highlight the importance of incorporating ensemble-based climate projections and non-stationary extreme-event behaviour into future flood-risk assessments and planning frameworks.

Conclusions

This study examined the projected evolution of groundwater flooding in a lowland karst system under contrasting climate-change emission pathways by integrating Bayesian Neural Network (BNN) flood modelling with ensemble climate projections and multi-scale statistical analyses. The combined use of trend analysis, wavelet coherence, antecedent rainfall diagnostics, and extreme-value modelling provides a comprehensive and internally consistent assessment of how both the magnitude and drivers of flooding respond to future climate forcing.

The results consistently indicate a strong dependence of future flood behaviour on emission pathway. Across all analyses, higher greenhouse-gas forcing (RCP8.5) leads to systematically larger and more frequent high-volume flood events compared to the stabilised-emissions pathway (RCP4.5). Probabilistic BNN outputs show an increased likelihood of extreme flood volumes under RCP8.5, with exceedances of the early-century 95th percentile occurring substantially more often than under RCP4.5. Upper-tail diagnostics—including annual maxima, rolling percentiles, and decadal distributions—demonstrate that flood extremes intensify not only in magnitude but also in frequency, with RCP8.5 exhibiting earlier emergence of high-impact conditions and a broader seasonal window of elevated flood risk.

Time–frequency analysis using wavelet coherence highlights rainfall as the dominant driver of groundwater flooding across all ensembles, with stronger and more persistent coupling between rainfall variability and flood response under RCP8.5 than under RCP4.5. Tidal influences remain secondary but become more evident at longer time scales and in specific ensemble realisations under higher emissions, indicating an increased potential for compound flooding when elevated tides coincide with extreme rainfall. Importantly, analysis of tidal amplitude shows that the difference between daily high and low tides remains effectively stationary through the century under both emission pathways, implying that future tidal flood risk arises primarily from rising mean sea levels rather than from amplification of the tidal range itself.

Antecedent rainfall analyses further reveal that extreme groundwater floods are strongly conditioned by short-term pre-event wetting. Rainfall accumulated over several days immediately preceding an event exerts the strongest influence on peak flood volumes, while longer accumulation windows dilute this effect. Under RCP8.5, decadal shifts toward wetter baseline conditions increase the frequency with which catchments enter flood-prone states, thereby increasing the likelihood that intense rainfall translates into large groundwater floods.

Extreme-event and return-period analyses reinforce these findings. Under RCP8.5, extreme rainfall and flood events become both more frequent and more intense, with ensemble-mean increases of approximately 15–20% in event frequency and around 30% in mean extreme flood volume relative to RCP4.5. Generalized Extreme Value (GEV) analysis shows a pronounced compression of return periods under high emissions, with a historical 100-year daily rainfall event projected to occur on the order of once every 16 years by late century. This shift is driven primarily by an increase in exceedance probability rather than large increases in event magnitude, indicating that historical design thresholds are likely to underestimate future flood risk.

Limitations and future work

Several limitations should be acknowledged when interpreting these results. First, the BNN model exhibits systematic underprediction at the upper end of the flood-volume distribution on unseen data, a common limitation of data-driven models when extrapolating rare extremes. As a result, projected future flood magnitudes—particularly the most extreme events—should be regarded as conservative estimates. Second, uncertainties inherent in climate projections propagate through the hydrological simulations, as reflected by variability across ensemble members. While ensemble consistency supports the robustness of the identified trends, the precise magnitude and timing of changes remain uncertain.

Third, the analysis focuses on hydro-climatic drivers and does not explicitly account for potential future changes in land use, drainage infrastructure, groundwater abstraction, or adaptive flood-management interventions, all of which could modify local flood response. Finally, wavelet coherence identifies scale-dependent associations rather than causal mechanisms, and results should be interpreted as indicative of coupling strength rather than direct physical forcing.

Implications

Despite these limitations, the convergence of evidence across independent analytical approaches indicates that groundwater flood risk in lowland karst systems is likely to increase substantially under continued warming, particularly under high-emission pathways. The findings highlight the importance of incorporating ensemble-based climate projections, non-stationary extreme-event behaviour, and antecedent wetness effects into future flood-risk assessments. By explicitly quantifying how emission pathways influence flood magnitude, frequency,

and drivers, this study provides a robust scientific basis for evaluating future groundwater flood hazards under climate change.

Methods

To predict total flood volume based on rainfall and tidal volume data, a Bayesian Regularization Neural Network (BRNN) model was developed in MATLAB 2016a. The methodology comprised training the model using historical data and subsequently simulating future projections of flood volume based on climate scenarios. From 2007 to 2018, five turlough basins (Blackrock, Coy, Coole, Garryland, and Caherglassaun) were instrumented with pressure-transducer dataloggers (± 0.05 m) and surveyed their elevations (Trimble 4700 GPS, ± 0.01 m) to obtain hourly water-stage records. These water stages were converted to stored volumes using depth–area–volume polynomials derived from a merged LiDAR (2 m DEM, ± 0.15 m) and GPS-surveyed topography via kriging. Simultaneously, two tipping-bucket rain gauges (70 m and 150 m AOD) provided local rainfall data, gap-filled from the long-term Gort-Derrybrien gauge. Three rivers draining the Slieve Aughty hills were gauged using pressure transducers and periodic flow measurements to establish stage–discharge curves, capturing allogenic inflows into the karst network. Downstream, 15 min tide measurements at Galway Port supplied daily peak-tide boundary conditions. By summing each turlough's instantaneous storage, "total flood volume" was defined as the aggregate water stored across all five basins at any given time[41]. The model utilized rainfall and tidal level as key predictors; specifically, current day rainfall and lagged rainfall values from the four preceding days; current day tidal level and lagged tidal level values from the four preceding days. This configuration accounted for temporal dependencies in rainfall and tidal volume, which are critical drivers of flood volume. The BRNN model was trained on observed rainfall, tidal level, and total flood volume data spanning from 2009 to 2018. The total flood volume for each day was the output variable to be predicted. The neural network incorporated Bayesian regularization to prevent overfitting and improve generalizability. This approach penalized overly complex models by introducing prior distributions over the network parameters. The model architecture comprised a fully connected feedforward network with a single hidden layer of 100 neurons. Non-linear activation functions (e.g., ReLU) were employed to capture complex relationships between input features and flood volume. Bayesian regularization adjusted the weights during training to balance data fit and model complexity. This was achieved by minimizing an objective function that combined the mean squared error (MSE) and a regularization term proportional to the weight magnitudes:

$$L = MSE + \lambda \sum w^2 \tag{3}$$

where $\boldsymbol{\lambda}$= Regularization coefficient and w= Network weights.

After training the BRNN model, future flood volume projections were generated by simulating the model using rainfall and tidal level data derived from the Coordinated Regional Climate Downscaling Experiment (CORDEX). The rainfall inputs were taken from the EURO-CORDEX ensemble at 0.11° (~ 12 km) spatial resolution. While this is coarser than the point-scale rain gauge data used for model calibration, it represents the standard resolution for regional climate impact studies in Ireland. The CORDEX rainfall series were used without additional bias correction; however, calibration of the Bayesian neural network against long-term observations mitigates systematic biases. The CORDEX data encompassed projections under two representative concentration pathways (RCPs): RCP 4.5 (moderate emissions) and RCP 8.5 (high emissions). To further assess the consistency of climate forcing data, probability density functions (PDFs) of observed daily rainfall and tidal levels for the period 2007–2016 were compared with those derived from the corresponding CORDEX simulations. For rainfall, direct comparison of the observed and simulated series was undertaken, while for tidal levels the datasets were standardized (z-scores) to account for differing reference baselines prior to PDF estimation (Figures S19 and S20 of Supplementary Information). The comparison of observed and CORDEX-simulated daily rainfall distributions (Figure S19) shows broadly consistent shapes, both characterized by a right-skewed form and overlapping tails, confirming that the CORDEX ensemble reproduces the statistical characteristics of rainfall in the study area. Similarly, the standardized distributions of observed and simulated tidal levels (Figure S20) align closely in central tendency and spread, indicating that the CORDEX simulations capture the statistical behavior of tidal variability during the historical period. These analyses provide further confidence in the reliability of the CORDEX datasets as inputs to the Bayesian neural network model.

To further assess the reliability of the Bayesian neural network (BNN) model, we carried out independent validation and cross-validation analyses. Observed flood records were available for the period 2007–2016, which was used for model training and validation. First, we compared observed and simulated flood volumes for the independent period 2016–2018 at annual resolution (Figure S21). This comparison shows that, despite the short record length, the BNN model reproduces interannual variability reasonably well, with an R^2 of 0.82. Second, we evaluated model performance across the full observed record (2007–2016). The validation scatter (Figure S22) demonstrates strong agreement between observed and simulated flood volumes, with $R^2 = 0.93$ and NSE = 0.93. Finally, to test the robustness of the model calibration, we applied a 5-fold cross-validation to the 2007–2015 training dataset. The resulting performance metrics (Figure S23) show consistently high values ($R^2 \approx 0.996 \pm 0.0005$; NSE $\approx 0.996 \pm 0.0005$), confirming the stability of the BNN predictions across different subsets of the observed data.

The Bayesian neural network model simulated daily total flood volume projections from 2020 to 2100. Projections were performed for multiple ensembles to capture variability across climate models and emission scenarios. For each RCP scenario the daily ensemble-mean flood volume across all 11 Bayesian-neural-network members was computed. Time series was aggregated by calendar year and extracted the maximum flood volume in each year (2016–2100). To quantify long-term changes in peak magnitude, ordinary-least-squares linear trends

to the resulting annual-maxima series for both RCP4.5 and RCP8.5 was fitted. Using the early-century (2016–2034) daily ensemble-mean series from RCP4.5, the 95th-percentile flood-volume threshold was calculated. For each year of both RCP4.5 and RCP8.5, total number of days on which the daily ensemble-mean flood volume exceeded this fixed threshold was calculated, and plotted these counts versus year to illustrate changes in the frequency of high-impact flood days. To assess the presence of monotonic trends independent of distributional assumptions, non-parametric Mann–Kendall tests with Sen's slope estimation were applied to annual maximum flood volumes and annual counts of extreme-flood days for both emission scenarios.

To construct Fig. 3, the daily ensemble-mean flood volume for each RCP scenario by averaging across all 11 Bayesian-neural-network runs were computed. From these mean series the maximum flood volume in each calendar year (2016–2100) was extracted and grouped these annual maxima into decades (e.g. 2010 s, 2020 s, …). Side-by-side box-and-whisker diagrams for each decade—using green boxes for RCP 4.5 and red boxes for RCP 8.5—to illustrate shifts in the central tendency and spread of yearly peaks over time were plotted. Average monthly flood volume by grouping daily means into calendar months, separately for an early period (2016–2040) and a late period (2071–2100) was calculated. Solid lines denote RCP 4.5 and dashed lines RCP 8.5, with green for the early period and red for the late, revealing seasonal changes in flood climatology. 10-year (≈ 3 650-day) moving window to the daily ensemble-mean series and computed the 90th percentile within each window was applied. Plotting this rolling 90th-percentile time series (green for RCP 4.5, red for RCP 8.5) highlights long-term trends in high-end extremes.

The role of "priming" moisture by computing cumulative rainfall sums over rolling windows of 0–30 days before each flood event was quantified. Pearson correlations were then calculated between these antecedent sums and modelled flood volumes to identify the lag of maximum association. OLS regressions of the form given in Eq. 4 was fitted:

$$FloodVolume_t = \beta_0 + \beta_1 R_t + \beta_2 \sum_{i=1}^{n} R_{t-i} + \epsilon_t \tag{4}$$

for $n = 7$, 14, 30 days, and examined changes in R^2, coefficient magnitudes, and significance (p-values) to assess how much explanatory power antecedent wetness adds beyond same-day rainfall. β_0 is the intercept (the baseline flood volume when all rainfall predictors are zero). β_1 is the coefficient on R_t (same-day rainfall), quantifying how much Flood Volume$_t$ is expected to change per unit increase in today's rain, holding antecedent rain constant. β_2 is the coefficient on the cumulative antecedent sum $\sum_{i=1}^{n} R_{t-i}$ quantifying how much FloodVolume$_t$ changes per unit increase in the n-day antecedent rainfall total, holding same-day rain constant. ε_t is the error term (or residual) at time t, capturing all the variability in FloodVolume$_t$ not explained by the two rainfall predictors.

Wavelet coherence analysis was conducted to examine the temporal and frequency-domain relationships between rainfall, tidal level, and total flood volume. This method identifies the localized correlation between two time series across different timescales, providing insights into how these variables interact over time. The analysis was performed using MATLAB R2016a, leveraging its robust signal processing and wavelet analysis toolboxes. The continuous wavelet transform (CWT) was applied to each time series to decompose the data into time-frequency space. The CWT was computed using the Morlet wavelet, which provides an optimal balance between time and frequency resolution[42]. The transform produced wavelet coefficients that represent the magnitude and phase of the time series at different frequencies and time points. Wavelet coherence (R^2) measures the squared correlation between two wavelet transforms, defined as Eq. 5:

$$\mathrm{R}^2(\mathrm{s,t}) = \frac{\left|\mathrm{S}\left(\mathrm{W_{x,y}}\left(\mathrm{s,t}\right)\right)\right|^2}{\mathrm{S}\left(\left|\mathrm{W_x}\left(\mathrm{s,t}\right)\right|\right)^2 . \mathrm{S}\left(\left|\mathrm{W_y}\left(\mathrm{s,t}\right)\right|\right)^2} \tag{5}$$

where $W_x(s, t)$ and $W_y(s, t)$ are the wavelet transforms of the two time series x and y; $W_{x,y}(s, t)$ is the cross-wavelet transform and S represents a smoothing operator in both time and scale (s). The wcoherence function in MATLAB was used to compute the wavelet coherence between the two-time series (e.g., rainfall and total flood volume, tidal level, and total flood volume). The function outputs the coherence values R^2 for each combination of time (t) and scale (s), where coherence values range from 0 (no correlation) to 1 (perfect correlation).

To quantitatively analyse the long-term trends and extreme event behaviour of rainfall and total flood volume, a systematic mathematical framework in MATLAB was implemented. This methodology involved preprocessing, trend estimation, and extreme event characterization. The trend analysis was performed to estimate the linear and nonlinear changes in rainfall (R_t) and total flood volume (F_t) over the projection period (2020–2100). The time series data for rainfall and total flood volume were smoothed using a moving average filter:

$$X_t = \frac{1}{w} \sum_{i=t-w/2}^{t+w/2} X_i \tag{6}$$

where X_i is the raw data, w is the window size, X_t is the smoothed data. This operation was implemented in MATLAB using 'smoothdata' function. A linear regression model was fitted to the smoothed data to estimate the slope (m) and intercept (c). The smoothed data and fitted trends were plotted using the plot function in MATLAB to visualize the temporal patterns.

Flood events were defined using the daily total flood volume, computed as the sum of stage-derived volumes across the five instrumented turlough basins. We apply three complementary, reproducible metrics: (1) the annual maximum daily volume (one value per year) used for GEV/return-period analysis (baseline window

2018–2037; future window 2080–2099); (2) fixed 95th-percentile exceedances, where the 95% threshold is computed from the early-century reference ensemble (RCP4.5, 2016–2034) and every day above this fixed threshold is flagged as an extreme-flood day (annual counts are used to assess frequency changes); and (3) a 10-year moving 90th-percentile (≈ 3,650-day window) to reveal decadal shifts in the upper tail. We performed sensitivity and robustness checks — varying percentile thresholds (90%, 95%, 97.5%), applying declustering/minimum-dry-period rules for POT analyses, testing alternative GEV block lengths (e.g., 15–25 years) with bootstrap confidence intervals, and examining antecedent-wetness windows (7, 14, 30 days).

Extreme events were identified based on statistical thresholds and analysed for frequency and intensity trends. The 95th percentile threshold (T_{95}) was calculated for both rainfall and total flood volume using Eq. 7:

$$T_{95} = quantile(X, 0.95) \tag{7}$$

where X represents the rainfall and total flood volume data series. Data points exceeding the 95th percentile were flagged as extreme events. Scatter plots were generated to show the distribution of extreme events over time, with marker size or colour indicating event magnitude. The analysis was performed for multiple ensembles (e.g., Ensembles 1–11) to account for variability in climate projections. For each ensemble, the above methodology was applied, and results were aggregated to evaluate uncertainties and variations across scenarios (e.g., RCP 4.5 and RCP 8.5). This mathematical and MATLAB-based framework provided robust insights into long-term trends and the behaviour of extreme events in rainfall and total flood volume under projected climate conditions.

Decadal peak-tide analysis was performed to quantify how extreme tidal levels — driven by rising sea levels and potential changes in storm surge patterns — evolve under two contrasting emissions pathways. By aggregating annual maximum daily peak tides into full-decade bins, the intensity and variability of tidal extremes between RCP4.5 and RCP8.5 were directly compared. Daily "peak tide" levels were calculated by taking the maximum of each ensemble's five tide variables (T, T−1D, T−2D, T−3D, T−4D) on every modelled date for each RCP scenario (4.5 and 8.5) and each of the 11 Bayesian-NN ensembles. These daily peaks were averaged across all ensembles to produce an ensemble-mean daily peak tide time series for RCP4.5 and RCP8.5 from 2018 to 2100. The maximum daily peak tide in each calendar year to form two yearly-maximum series was extracted. Years were binned by decade (2010–2019, 2020–2029, …, 2090–2099), and within each decade side-by-side box-and-whisker plots were generated—green for RCP4.5 and red for RCP8.5—depicting the distribution of annual maximum peak tides. Increases in median or upper-whisker values under RCP8.5 indicate that higher greenhouse-gas forcing not only raises baseline water levels but also amplifies the most severe tide events. Understanding these shifts is critical for coastal infrastructure planning, flood-risk management, and adaptation strategies, because even small upward trends in annual peak tides can substantially increase overtopping risk, exacerbate groundwater flooding inland, and compound fluvial flood hazards. Estimating changes in return periods directly translates scientific projections into engineering and policy-relevant metrics ("100-year storm," "50-year flood," etc.) that communities use for floodplain zoning and infrastructure design. As greenhouse-gas forcing intensifies, the tail of the rainfall distribution shifts upward, shortening return periods of historically rare events. By explicitly fitting GEV distributions to annual maxima in two distinct 20-year windows, how the rarity of extreme storms evolves was quantified. This approach provides stakeholders with a clear, actionable picture of how often they can expect historically defined extremes to recur under future warming—information that is far more intuitive and decision-relevant than simply reporting mean or median changes.

Ensemble-mean daily rainfall for RCP8.5 by averaging the "R" column across all 11 Bayesian-NN ensemble members for each date from 2018 to 2100 were computed. Two non-overlapping 20-year windows: the "baseline" (2018–2037) and "future" (2080–2099) were selected. For each window, the annual maximum of the ensemble-mean daily rainfall (one value per year) to create two 20-point series of annual maxima were extracted. Each series was fit to a three-parameter Generalized Extreme-Value (GEV) distribution using SciPy's genextreme.fit routine. For each scenario (RCP 4.5 and RCP 8.5) and each 11-member ensemble, the ensemble-mean daily rainfall (or flood volume) time series were computed. This series was partitioned into two 20-year windows: baseline (2018–2037) and future (2080–2099). Within each window, the annual maximum value for each calendar year was extracted, yielding two samples of 20 block maxima per scenario. The GEV probability distribution to each 20-point block-maxima sample was fitted. The GEV cumulative distribution function is:

$$F(x;\xi,\mu,\sigma) = \exp\left\{-\left[1+\frac{\xi\,(x-\mu)}{\sigma}\right]^{\frac{-1}{\xi}}\right\}, for 1+\frac{\xi(x-\mu)}{\sigma} > 0, \tag{8}$$

Where, μ is the location parameter (shift of the distribution), σ > 0 is the scale parameter (spread), and $\boldsymbol{\xi}$ is the shape parameter. For each baseline and future sample, the fitted parameter values and assess fit quality via the Kolmogorov–Smirnov statistic and QQ-plots of empirical versus theoretical quantiles were recorded.

The GEV family comprises three distinct types determined by the shape parameter ξ.

1. Type I (Gumbel) (ξ = 0).

$$F(x) = exp(-e^{-\frac{x-\mu}{\sigma}}), x\mathrm{d}R, \tag{9}$$

2. Type II (Fréchet) (ξ > 0).

$$F(x) = \begin{cases} \exp\left\{-\left[1+\frac{\xi(x-\mu)}{\sigma}\right]^{\frac{-1}{\xi}}\right\} & , x > \mu - \frac{\sigma}{\xi}, \\ 0, & x \le \mu - \frac{\sigma}{\xi}. \end{cases} \tag{10}$$

3. Type III (Weibull) ($\xi < 0$).

$$F(x) = \begin{cases} \exp\left\{-\left[1+\frac{\xi(x-\mu)}{\sigma}\right]^{\frac{-1}{\xi}}\right\} & , x < \mu - \frac{\sigma}{\xi}, \\ 1, & x \ge \mu - \frac{\sigma}{\xi}. \end{cases} \tag{11}$$

In all cases, μ is the location, $\sigma > 0$ the scale, and ξ the shape parameter that controls tail behavior.

Return levels X_T (rainfall thresholds) for return periods T= {2,5,10,20,50,100,200}years were computed by solving:

$$F_{GEV}(X_T) = 1 - \frac{1}{T} \tag{12}$$

where F_{GEV} is the fitted GEV cumulative distribution function. This yielded two return-period curves (baseline and future), which was plotted on a logarithmic x-axis. Finally, evaluation of how the baseline's 100-year return level maps onto a shorter return period under the future GEV were computed using below given equation:

$$T_{future} = \left[1 - F_{GEV,future}\left(X_{100,baseline}\right)\right]^{-1} \tag{13}$$

20-year non-overlapping windows (2018–2037) were chosen to ensure enough annual maxima for robust estimation but avoid mixing mid-century dynamics. Because each GEV fit is based on only 20 maxima, 95% confidence intervals on x_T via the profile-likelihood method implemented in scipy.stats.genextreme.confidence_ interval were estimated. Sensitivity tests were performed by varying the block length (e.g., 15-year vs. 25-year windows) and by bootstrapping the block-maxima samples to ensure robustness of the observed return-period shifts. By applying this GEV-based framework separately to RCP 4.5 and RCP 8.5, quantitative evidence that under high greenhouse-gas forcing, flood and rainfall extremes intensify (vertical shift) and their return periods compress (horizontal shift), providing decision-relevant metrics such as: "what was a 1-in-100-year storm in 2018–2037 becomes a 1-in-16-year event by 2080–2099 under RCP 8.5", were obtained.

Data availability

The datasets used in this study, including rainfall and tidal level projections from CORDEX simulations and total flood volume predictions from the Bayesian Neural Network model, are available upon reasonable request. Access to the CORDEX datasets is subject to the data-sharing policies of the Coordinated Regional Downscaling Experiment. Derived datasets generated during the study are also available from the corresponding author on reasonable request.

Received: 30 June 2025; Accepted: 6 March 2026
Published online: 17 March 2026

References

1. Zscheischler, J. et al. Future climate risk from compound events. *Nat. Clim. Change* **8**, 469–477. https://doi.org/10.1038/s41558-018-0156-3 (2018).
2. Bevacqua, E., Maraun, D., Hobæk Haff, I., Widmann, M. & Vrac, M. Multivariate statistical modelling of compound events via pair-copula constructions: Analysis of floods in Ravenna (Italy). *Hydrol. Earth Syst. Sci.* **21**, 2701–2723 (2017).
3. Gill, L. W., Naughton, O. & Johnston, P. M. Modeling a network of turloughs in lowland karst. *Water Resour. Res.* **49**, 3487–3503 (2013).
4. Naughton, O., Mccormack, T., Gill, L. & Johnston, P. Groundwater flood hazards and mechanisms in lowland karst terrains. *Geol. Soc. Spec. Publ.* **466**, 397–410 (2018).
5. Naughton, O., Johnston, P. M. & Gill, L. W. Groundwater flooding in Irish karst: The hydrological characterisation of ephemeral lakes (turloughs). *J. Hydrol.* **470–471**, 82–97 (2012).
6. Morrissey, P. et al. Impacts of climate change on groundwater flooding and ecohydrology in lowland karst. *Hydrol. Earth Syst. Sci.* **25**, 1923–1941 (2021).
7. Olbert, A. I. et al. Combined statistical and hydrodynamic modelling of compound flooding in coastal areas - Methodology and application. *J. Hydrol.* **620**, 129383 (2023).
8. Donges, J. F., Schleussner, C. F., Siegmund, J. F. & Donner, R. V. Event coincidence analysis for quantifying statistical interrelationships between event time series: on the role of flood events as possible triggers of epidemic outbreaks. (2015). https://doi.org/10.1140/epjst/e2015-50233-y
9. Prudhomme, C., Wilby, R. L., Crooks, S., Kay, A. L. & Reynard, N. S. Scenario-neutral approach to climate change impact studies: Application to flood risk. *J. Hydrol.* **390**, 198–209 (2010).
10. Roudbari Shafiee, N., Punekar Rajeev, S., Patterson, Z., Eicker, U. & Charalambos, P. From data to action in flood forecasting leveraging graph neural networks and digital twin visualization. *Sci. Rep.* https://doi.org/10.1038/s41598-024-68857-y (2024).
11. Mishra, V., Bhatia, U. & Tiwari, A. D. Bias-corrected climate projections for South Asia from Coupled Model Intercomparison Project-6. *Sci. Data* https://doi.org/10.1038/s41597-020-00681-1 (2020).
12. Im, E.-S., Pal, J. S. & Eltahir, E. A. B. Deadly heat waves projected in the densely populated agricultural regions of South Asia. *Sci. Adv.* https://doi.org/10.1126/sciadv.1603322 (2017).
13. Hartmann, A. et al. Process-based karst modelling to relate hydrodynamic and hydrochemical characteristics to system properties. *Hydrol. Earth Syst. Sci.* **17**, 3505–3521 (2013).

14. Hartmann, A. et al. A large-scale simulation model to assess karstic groundwater recharge over Europe and the Mediterranean. *Geosci. Model Dev.* **8**, 1729–1746 (2015).
15. Bottrell, S. H., Ford, D. & Williams, P. Karst geomorphology and hydrology. *Geogr. J.* https://doi.org/10.2307/635167 (1991).
16. Jeannin, P. Y. et al. Karst modelling challenge 1: Results of hydrological modelling. *J. Hydrol.* **600**, 126508 (2021).
17. Al-Rawas, G. et al. Near future flash flood prediction in an arid region under climate change. *Sci. Rep.* https://doi.org/10.1038/s41598-024-76232-0 (2024).
18. Zennaro, F. et al. Exploring machine learning potential for climate change risk assessment. *Earth Sci. Rev.* https://doi.org/10.1016/j.earscirev.2021.103752 (2021).
19. Guntu, R. K., Maheswaran, R., Agarwal, A. & Singh, V. P. Accounting for temporal variability for improved precipitation regionalization based on self-organizing map coupled with information theory. *J. Hydrol.* https://doi.org/10.1016/j.jhydrol.2020.125236 (2020).
20. Gallina, V. et al. A review of multi-risk methodologies for natural hazards: Consequences and challenges for a climate change impact assessment. *J. Environ. Manage.* **168**, 123–132. https://doi.org/10.1016/j.jenvman.2015.11.011 (2016).
21. Gill, L. W., Naughton, O., Johnston, P. M., Basu, B. & Ghosh, B. Characterisation of hydrogeological connections in a lowland karst network using time series analysis of water levels in ephemeral groundwater-fed lakes (turloughs). *J. Hydrol.* **499**, 289–302 (2013).
22. Wang, W., Ye, F., Wang, Y. & Gu, M. A singular spectrum analysis-enhanced BiTCN-selfattention model for runoff prediction. *Earth Sci. Inform.* https://doi.org/10.1007/s12145-024-01524-y (2025).
23. Sidhan, V. V. & Singh, S. Multiscale association between large-scale climate variability modes and drought in India via wavelet analysis. *Int. J. Climatol.* https://doi.org/10.1002/joc.8435 (2024).
24. Das, J., Jha, S. & Goyal, M. K. On the relationship of climatic and monsoon teleconnections with monthly precipitation over meteorologically homogenous regions in India: Wavelet & global coherence approaches. *Atmos. Res.* https://doi.org/10.1016/j.atmosres.2020.104889 (2020).
25. Miklós, R. et al. Karst water resources and their complex utilization in the Bükk Mountains, northeast Hungary: An assessment from a regional hydrogeological perspective. *Hydrogeol. J.* **28**, 2159–2172 (2020).
26. Hall, J. et al. Understanding flood regime changes in Europe: A state-of-the-art assessment. *Hydrol. Earth Syst. Sci.* **18**, 2735–2772 (2014).
27. Peña, F. et al. Compound flood modeling framework for surface-subsurface water interactions. *Nat. Hazards Earth Syst. Sci.* **22**, 775–793 (2022).
28. Beniston, M. Trends in joint quantiles of temperature and precipitation in Europe since 1901 and projected for 2100. *Geophys. Res. Lett.* https://doi.org/10.1029/2008GL037119 (2009).
29. Shepherd, T. G. et al. Storylines: An alternative approach to representing uncertainty in physical aspects of climate change. *Clim. Change* **151**, 555–571 (2018).
30. Beniston, M. et al. Future extreme events in European climate: An exploration of regional climate model projections. *Clim. Change* **81**, 71–95. https://doi.org/10.1007/s10584-006-9226-z (2007).
31. Trenberth, K. E. & Shea, D. J. Relationships between precipitation and surface temperature. *Geophys. Res. Lett.* **32**, 1–4 (2005).
32. Bevacqua, E. et al. Guidelines for studying diverse types of compound weather and climate events. *Earths Future* https://doi.org/10.1029/2021EF002340 (2021).
33. Boers, N. et al. Complex networks reveal global pattern of extreme-rainfall teleconnections. *Nature* **566**, 373–377 (2019).
34. Russo, S. et al. Magnitude of extreme heat waves in present climate and their projection in a warming world. *J. Geophys. Res. Atmos.* **119**, 12,500-12,512 (2014).
35. Hao, Z., Singh, V. P. & Hao, F. Compound extremes in hydroclimatology: A review. *Water* https://doi.org/10.3390/w10060718 (2018).
36. Rehana, S., Yeleswarapu, P., Basha, G. & Munoz-Arriola, F. Precipitation and temperature extremes and association with large-scale climate indices: An observational evidence over India. *J. Earth Syst. Sci.* https://doi.org/10.1007/s12040-022-01911-3 (2022).
37. Rathinasamy, M., Agarwal, A., Sivakumar, B., Marwan, N. & Kurths, J. Wavelet analysis of precipitation extremes over India and teleconnections to climate indices. *Stoch. Environ. Res. Risk Assess.* **33**, 2053–2069 (2019).
38. Tabbussum, R., Bhowmik, R. D. & Mujumdar, P. Association of climate variability modes with concurrent droughts and heatwaves in India. *J. Hydrol. X* **26**, 100196 (2025).
39. Aghakouchak, A. et al. Climate extremes and compound hazards in a warming world. *Annu. Rev. Earth Planet. Sci.* **48**, 519–567 (2020).
40. Torrence, C. & Compoher, G. P. *A Practical Guide to Wavelet Analysis*. vol. 32 (1997).
41. Basu, B., Morrissey, P. & Gill, L. W. Application of nonlinear time series and machine learning algorithms for forecasting groundwater flooding in a lowland karst area. *Water Resour. Res.* **58**, 1–30 (2022).
42. Torrence, C. & Compo, G. P. A practical guide to wavelet analysis. *Bull. Am. Meteorol. Soc.* **79**, 61–78 (1998).

Acknowledgements

The authors would like to thank the Environmental Protection Agency for funding the research, as part of the Water Futures project (EPA ref. 2020-W-CD-3).

Author contributions

Ruhhee Tabbussum: Conceptualization, Methodology, Software, Analysis, Original draft preparation, Revised draft preparation, Visualization, Validation. Bidroha Basu: Writing- Reviewing and Editing. Patrick Morrisey: Data curation, Writing- Reviewing and Editing. Conor Murphy: CORDEX Data curation, Writing- Reviewing and Editing. Laurence Gill: Supervision, Data Curation, Validation, Writing- Reviewing and Editing.

Funding

This research was funded by the Environmental Protection Agency (EPA) of Ireland as part of the Water Futures project (EPA-2020-W-CD-3).

Declarations

Competing interests

The authors declare no competing interests.

Additional information

Supplementary Information The online version contains supplementary material available at https://doi.org/1

0.1038/s41598-026-43701-7.

Correspondence and requests for materials should be addressed to R.T.